# Accurate Modelling and Simulation of Thermomechanical Microsystem Dynamics

**S. Taschini[1], J. Müller[2], A. Greiner[2], M. Emmenegger[1], H. Baltes[1], J.G. Korvink[2]**

**Abstract:** We present three techniques to accurately model the thermomechanical response of microsystem components: a new, accurate and stable Kirchhoff-Love multi-layered plate model implemented as an Argyris finite element, a model for the amplitude fluctuations of vibrational modes in micromechanical structures within a gaseous environment, and the consistent refinement of a finite element mesh in order to maximize the computational accuracy for a given mesh size. We have implemented these techniques in our in-house MEMS finite element program and accompanying Monte Carlo simulator. We demonstrate our approach to dynamic modeling by computing the thermomechanical response of a CMOS AFM beam.

**keyword:** microsystems, finite elements, plate theory, fluctuations, refinement

## 1 Introduction

Dynamic microsystems provide the designer with a wide spectrum of techniques in the time and frequency domains for both sensing and actuation. They also fit naturally in systems, especially integrated circuits, where the signal conditioning is performed using advanced designs for noise reduction, offset and drift compensation. They also pose new problems for their simulation, due to the strong coupling between different energy domains, to the scaling of the physical phenomena, to the large aspect-ratio of the components, and to their typical time constants.

Semiconductor technology produces mechanical microsystem components shaped into plate or beam-like structures and composed of multi-layer sandwiches. It is essential to have a reliable, stable discretization scheme for these thermally prestressed material stacks that enables the use of small meshes. To further reduce the computational cost for a given degree of accuracy, methods are needed to automatically adapt the computational mesh there where the accuracy is required. As microsystem components reduce in size, they tend to become mesoscopic, and as a result the characterization of random fluctuations inherent in physical processes becomes important.

In this paper we address these aspects. We are driven by the need to design and characterize a noise-suppressing, CMOS-based atomic force microscope beam [Lange, Akiyama, Hagleitner, Tonin, Hidber, Niedermann, Staufer, de Rooij, Brand, and Baltes (1999)]. To this end we have designed and implemented a new multi-layer Kirchhoff-Love plate finite element that exhibits a high degree of accuracy and is largely insensitive to the quality of the finite element mesh. In Sec. 2 we develop the three-dimensional Lagrangian thermomechanics in a form that lends itself to the derivation of plate theory. In Sec. 3 the 3D model is specialized to the case of thermomechanical plates by deriving a weak form from the Lagrangian partial differential equations. The discretization for the element is done following a conforming finite element interpolation, and is implemented using Argyris elements [Argyris, Fried, and Scharpf (1968)]. With the new model, we are able to accurately extract the vibrational modes of the AFM beams. In Sec. 4 we apply the Dissipation-Fluctuation theorem to thermomechanical structures and obtain the noise behavior of the AFM beam when randomly excited by a gaseous environment. Using the vibrational modes of the beam as a starting point, amplitude fluctuations are computed with a Monte Carlo technique. In Sec. 5 we discuss finite element mesh adaptivity as a process that requires an error estimator, a refinement strategy and a mesh splitting method. In Sec. 6 the techniques presented are combined and applied to a CMOS AFM beam currently under development [Lange, Akiyama, Hagleitner, Tonin, Hidber, Niedermann, Staufer, de Rooij, Brand, and Baltes (1999)].

## 2 Three-dimensional thermomechanics

The model presented here is derived in the context of the continuum hypothesis, whereby any physical quantity is represented by a field that defines its value at any position in space. Even at the level of microsystems, the continuum hypothesis is by far justified, for the characteristic lengths of the system are more than two orders of magnitude larger than the molecular size or than the crystalline step [Nathan and Baltes (1999)]. Nevertheless, the quantities involved in the continuum theory are closely related to the quantities in the solid-state theory. In a crystal, the cohesive energy of the lattice, given by the sum of the binding energies of the ions, becomes in the continuum limit the (Helmholtz) free energy of the body. In the crystal, the physical quantities are associated with the ions forming the lattice, which is discrete in nature. Therefore $m_i$, $\mathbf{x}_i$, and $\mathbf{u}_i$ describe the mass, the position, and the displacement of the ion with index $i$. Similarly, the binding energy is evaluated at the discrete positions given by the displaced positions of the ions. For the continuum case, the displacement is described by the

[1] Physical Electronics Laboratory, ETH Zürich, Switzerland
[2] IMTEK, University of Freiburg, Germany

field $\mathbf{u}(\mathbf{x})$ whereas the mass and the free energy are represented by their densities $\rho(\mathbf{x})$ and $\phi(\mathbf{x})$.

### 2.1 Lagrangian and hamiltonian formulation

The lattice lagrangian [Ashcroft and Mermin (1976)]

$$\hat{L}_L = \frac{1}{2}\sum_i m_i \left(\dot{\mathbf{x}}_i + \dot{u}_i\right)^2 - \frac{1}{2}\sum_{ij}\phi\left(\mathbf{x}_i + \mathbf{u}_i - \mathbf{x}_j - \mathbf{u}_j\right) \tag{1}$$

becomes in the limit the continuum lagrangian

$$\hat{L} = \int_\Omega \left(\rho\dot{\mathbf{u}}^2/2 - \phi(\mathbf{u})\right) \mathrm{d}^3x \tag{2}$$

The displacement maps a point $\mathbf{x}$ onto the point $\mathbf{x}' = \mathbf{x} + \mathbf{u}(\mathbf{x})$ and the vector $d\mathbf{x}$ between two infinitesimally close points is mapped onto the differential $d\mathbf{x}' = d\mathbf{x} + d\mathbf{x}\cdot\nabla\mathbf{u}$. The notation adopted is that the dot signifies the contraction between tensors and the dyadic notation signifies the tensor product [Gibbs and Wilson (1901)]. The notation for the symmetrization of a second order tensor $A$ is introduced as

$$A^S = \frac{A + A^T}{2} \tag{3}$$

in analogy with the transposition. The deformation of the solid medium is given by the change of the distance between two infinitesimally close vectors, namely

$$\left(\mathrm{d}\mathbf{x}'\right)^2 - \left(\mathrm{d}\mathbf{x}\right)^2 = 2\,\mathrm{d}\mathbf{x}\cdot\left[(\nabla\mathbf{u})^S + \frac{1}{2}(\nabla\mathbf{u})\cdot(\nabla\mathbf{u})^T\right]\cdot\mathrm{d}\mathbf{x} \tag{4}$$

The symmetric second-order tensor inside the square brackets determines the state of the deformation and defines the (Green-St. Venant) tensor $\varepsilon$

$$\varepsilon = (\nabla\mathbf{u})^S + \frac{1}{2}\nabla\mathbf{u}\cdot(\nabla\mathbf{u})^T \tag{5}$$

which is a non linear function of $\nabla\mathbf{u}$. For a non-dispersive elastic continuum, the (Helmholtz) free energy density $\phi(\varepsilon, T)$ is a function of the strain and of the temperature, the latter dependency implying an anharmonic binding energy. The derivatives of the free energy define the static (second Piola-Kirchhoff) stress tensor and the entropy density

$$\sigma = \partial\phi/\partial\varepsilon \tag{6}$$

$$\eta = -\partial\phi/\partial T \tag{7}$$

The internal energy is minus the Legendre transform of the free energy with respect to the temperature

$$e = \phi - T\partial\phi/\partial T \tag{8}$$

which is expressed as a function of the independent variables $\varepsilon$, $T$ as

$$e(\varepsilon, T) = \phi(\varepsilon, T) + T\eta(\varepsilon, T) \tag{9}$$

Taking its derivative with respect to the temperature determines the clamped, i.e. at constant strain, heat capacity

$$c = \frac{\partial e}{\partial T} = \frac{\partial\phi}{\partial T} + \eta + T\frac{\partial\eta}{\partial T} = T\frac{\partial\eta}{\partial T} \tag{10}$$

Taking the total time derivative of the entropy yields the relation

$$\dot{\eta}(\varepsilon, T) = \frac{\partial\eta}{\partial T}\dot{T} + \frac{\partial\eta}{\partial\varepsilon} : \dot{\varepsilon} = c\frac{\dot{T}}{T} - \frac{\partial^2\phi}{\partial T\partial\varepsilon} : \dot{\varepsilon} = c\frac{\dot{T}}{T} - \frac{\partial\sigma}{\partial T} : \dot{\varepsilon} \tag{11}$$

The role of the temperature as the pivot for the Legendre transform between the internal and the free energy, makes the temperature act like a rate in the lagrangian density stemming from Eq. 2

$$L(\mathbf{q}, \dot{\mathbf{q}}, \nabla\mathbf{q}) = \frac{1}{2}\rho\dot{\mathbf{u}}^2 - \phi(\varepsilon, T) \tag{12}$$

Introducing $\theta$ as the time primitive of the temperature, i.e. satisfying $T = \dot{\theta}$, the four-dimensional vector $\mathbf{q}$ is

$$\mathbf{q} = (\mathbf{u}, \theta) \tag{13}$$

The Euler-Lagrange equations

$$\frac{\mathrm{d}}{\mathrm{d}t}\left(\frac{\partial L}{\partial\dot{\mathbf{q}}}\right) + \nabla\cdot\left(\frac{\partial L}{\partial\nabla\mathbf{q}}\right) - \frac{\partial L}{\partial\mathbf{q}} = 0 \tag{14}$$

applied to the lagrangian density (Eq. 12) yield the system of PDEs

$$\begin{cases} \rho\ddot{\mathbf{u}} - \nabla\cdot\left(\dfrac{\partial\phi}{\partial\nabla\mathbf{u}}\right) = 0 \\ \dot{\eta} = 0 \end{cases} \tag{15}$$

The first equation expresses the conservation of momentum and is further manipulated using the identity

$$\left(\frac{\partial\phi}{\partial\nabla\mathbf{u}}\right)_{ij} = \frac{\partial\phi}{\partial\varepsilon_{kl}}\frac{\partial\varepsilon_{kl}}{\partial\mathbf{u}_{j,i}} = \left[\sigma\cdot(1 + \nabla\mathbf{u})\right]_{ij} \tag{16}$$

into

$$\rho\ddot{\mathbf{u}} - \nabla\cdot\left[\sigma\cdot(1 + \nabla\mathbf{u})\right] = 0 \tag{17}$$

Even in the presence of a material with linear constitutive relations, this equation is nonlinear, partly because of the non linearity of the strain $\varepsilon$ with respect to the displacement $\mathbf{u}$, partly because of the contraction between the stress and the gradient of the displacement inside the argument of the divergence. The second equation of the system (Eq. 15) signifies that the process is adiabatic, and thanks to the thermodynamic identity (Eq. 11), can be used to get the equation for the temperature

$$c\dot{T} = T\frac{\partial\sigma}{\partial T} : \dot{\varepsilon} \tag{18}$$

The hamiltonian density $H$ is defined by the Legendre transform of the lagrangian density,

$$H = \frac{\partial L}{\partial \dot{\mathbf{q}}} \cdot \dot{\mathbf{q}} - L = \rho \dot{\mathbf{u}}^2 + T\eta - L = \frac{1}{2}\rho \dot{\mathbf{u}}^2 + e \tag{19}$$

which, not surprisingly, coincides with the energy density. Actually, the hamiltonian density as a function of the generalized coordinate field $(\mathbf{u}, \theta)$ and of its conjugate moments $(\rho\mathbf{u}, \eta)$, can be taken as the starting point and the lagrangian density (Eq. 12) can be recovered via a Legendre transform.

The Hamilton principle

$$\delta \int_{t_1}^{t_2} L \mathrm{d}t = 0 \tag{20}$$

equivalent to the system (Eq. 15) can be extended for a dissipative system experiencing external solicitations, by including the action associated with the virtual work $W$ of the additional generalized forces.

$$\delta \int_{t_1}^{t_2} L \mathrm{d}t + \int_{t_1}^{t_2} W \mathrm{d}t = 0 \tag{21}$$

### 2.2 The weak form

Depending of the type of phenomena that are taken into consideration the expression for the virtual work $W$ can vary considerably. For the virtual work of the mechanical forces, considering only the effect of an impressed volume force density and of a surface boundary force density acting on the boundary of the solid, the virtual work is

$$W_M = \int_\Omega f_v \cdot \delta\mathbf{u} \, \mathrm{d}^3\mathbf{x} + \int_{\partial\Omega} f_s \cdot \delta\mathbf{u} \, \mathrm{d}S(\mathbf{x}) \tag{22}$$

If the heat transfer is considered as the only irreversible process in the solid, its virtual work is given in terms of the inbound entropy flow and in terms of a net increase of entropy

$$W_T = \int_\Omega \frac{\nabla T \cdot k \cdot \nabla T}{T^2} \delta\theta \, \mathrm{d}^3 x - \int_{\partial\Omega} \frac{\mathbf{n} \cdot \mathbf{Q}}{T} \delta\theta \, \mathrm{d}S(\mathbf{x}) \tag{23}$$

The first of the two integrals is a quadratic form in which the Fourier law for heat transfer has been used. The fact that it expresses the net generation of entropy, which must be positive in accordance with the second law of thermodynamics, poses a thermodynamic constraint on the positivity of the thermal conductivity second-order tensor. The second integral in Eq. 23 represents the interaction with the environment by means of the heat flux $\mathbf{Q}$, and using the theorem of the divergence, can be put in the form of a volume integral. Eventually the thermal virtual work has the form

$$\begin{aligned} W_T &= \int_\Omega \left[ \frac{\nabla T \cdot k \cdot \nabla T}{T^2} - \nabla \cdot \left( \frac{\mathbf{Q}}{T} \right) \right] \delta\theta \, \mathrm{d}^3 x \\ &= \int_\Omega \left[ \frac{\nabla T \cdot (k \cdot \nabla T + \mathbf{Q})}{T^2} - \frac{\nabla \cdot \mathbf{Q}}{T} \right] \delta\theta \, \mathrm{d}^3 x \\ &= -\int_\Omega \frac{\nabla \cdot \mathbf{Q}}{T} \delta\theta \, \mathrm{d}^3 x \end{aligned} \tag{24}$$

Carrying out the variational derivative in Eq. 21 yields the system

$$\begin{cases} \rho\ddot{\mathbf{u}} - \nabla \cdot [\sigma \cdot (1 + \nabla\mathbf{u})] = f_v + f_s \delta_{\partial\Omega} \\ \dot{\eta} + \dfrac{\nabla \cdot \mathbf{Q}}{T} = 0 \end{cases} \tag{25}$$

The second equation can be expressed in terms of the temperature thus yielding from Eq. 11 the equation

$$c\dot{T} = T \frac{\partial}{\partial T}(\sigma) : \dot{\varepsilon} - \nabla \cdot \mathbf{Q} \tag{26}$$

Also the so-called weak form of the thermomechanical initial-condition boundary-value problem stems directly from Eq. 21. Indeed, using the anti-symmetry of the time-derivative inside the integral, the variation of the action can be cast as

$$\begin{aligned} \delta \int_{t_1}^{t_2} L \mathrm{d}t &= \delta \int_{t_1}^{t_2} \int_\Omega \left( \rho \dot{\mathbf{u}}^2/2 - \phi \right) \mathrm{d}^3 x \mathrm{d}t \\ &= \int_{t_1}^{t_2} \int_\Omega \left( \rho\dot{\mathbf{u}} \cdot \delta\mathbf{u} - \sigma : \delta\varepsilon + \eta\delta T \right) \mathrm{d}^3 x \mathrm{d}t \\ &= \int_{t_1}^{t_2} \int_\Omega \left( -\rho\mathbf{u} \cdot \delta\mathbf{u} - \sigma : \delta\varepsilon - \dot{\eta}\delta\theta \right) \mathrm{d}^3 x \mathrm{d}t \end{aligned} \tag{27}$$

Using the more expressive formalism of the inner product in $L^2(\Omega)$, the space of square integrable tensor valued functions, or its generalization for distributions, for the variation of the action, the variational principle Eq. 21 is then recast as

$$\int_{t_1}^{t_2} \left[ (\rho\ddot{\mathbf{u}}, \delta\mathbf{u}) + (\sigma, \delta\varepsilon) + (\dot{\eta}, \delta\theta) \right] \mathrm{d}t = \int_{t_1}^{t_2} W \mathrm{d}t \tag{28}$$

Since this equation must be satisfied for all possible variations of the independent fields, the two expressions under integration must be equal, and the weak form is then

$$\begin{aligned} (\rho\ddot{\mathbf{u}}, \delta\mathbf{u}) + (\sigma, \delta\varepsilon) + (\dot{\eta}, \delta\theta) &= (f_v, \delta\mathbf{u}) + (f_s, \delta\mathbf{u})_{\partial\Omega} \\ &+ \left( \nabla T \cdot k \cdot \nabla T / T^2, \delta\theta \right) - (\mathbf{Q} \cdot \mathbf{n}, \delta\theta)_\Omega \end{aligned} \tag{29}$$

### 2.3 Constitutive parameters

For a linear material the constitutive equation (Eq. 6) becomes

$$\sigma = A : (\varepsilon - \alpha T) \tag{30}$$

where $A$ is the fourth-order elastic tensor, $\sigma$ the stress, $\alpha$ is the second-order thermal expansion tensor, and for convenience $T$ is the offset temperature from the stress-free temperature $T_0$. The derivative of the constitutive equation (Eq. 30) with respect to a component of the strain

$$A_{ijkl} = \frac{\partial \sigma_{ij}}{\partial \varepsilon_{kl}} = \frac{\partial^2 \phi}{\partial \varepsilon_{kl} \partial \varepsilon_{ij}} \tag{31}$$

yields the symmetry between the first and the second pair of indices

$$A_{ijkl} = A_{klij} \tag{32}$$

Integrating the stress (Eq. 30) with respect to the strain and using the symmetries of the elastic tensor the yields the free energy

$$\phi(\varepsilon, T) = \frac{1}{2}\varepsilon : A : \varepsilon - \varepsilon : A : \alpha T + \phi_0(T) \tag{33}$$

The strain tensor is symmetric by the definition (Eq. 5), and therefore the elastic tensor exhibits the symmetry of the last two indices

$$A_{ijkl} = A_{ijlk} \tag{34}$$

which combined with Eq. 32 yields the symmetry of the first two indices

$$A_{ijkl} = A_{jikl} \tag{35}$$

These symmetries reduce the number of independent parameters in the elastic tensor from 81 to 36, and further constraints are introduced by the Neumann principle, which states that all the tensors expressing material properties, such as the elastic tensor, must be invariant with respect to the point-group symmetries of the material [Nye (1985)]. Similar considerations hold for the thermal expansion coefficient, which must be symmetric, as is implied by the constitutive equation (Eq. 30). In the case of an isotropic material only two independent parameters are left in the elastic tensor whereas only one parameter is left in the thermal expansion coefficient. In terms of the Young modulus E and the Poisson ratio ν [Landau and Lifshitz (1986)]

$$A_{ijkl} = \frac{E}{1+\nu}\left(\frac{1}{2}\delta_{ik}\delta_{jl} + \frac{1}{2}\delta_{il}\delta_{jk} + \frac{\nu}{1-2\nu}\delta_{ij}\delta_{kl}\right) \tag{36}$$

thermal expansion coefficient simply reduces to a scalar, and the stress-strain relation becomes

$$\sigma = \frac{E}{1+\nu}\left(\varepsilon + \frac{\nu\ \mathrm{tr}\varepsilon}{1-2\nu}\right) - \frac{E\alpha T}{1-2\nu} \tag{37}$$

## 3 Multi-layered kirchhoff-love plates

Either the lagrangian formulation (Eq. 21) or the weak formulation (Eq. 29) of three-dimensional thermomechanics can be taken as the starting point for further development such as linearization or limit operations. In particular, plate models are obtained as the asymptotic case for one of the dimensions of the solid vanishing (Fig. 1). These operations of limit and linearization are in general non commutative. Terms neglected in the linearization might have been dominant in the limit. Therefore to get the linear theory of plates it is necessary first to deduce the non-linear theory and then to linearize it. In the asymptotic case for plates, the unknown field is assumed a priori to have a polynomial dependence with respect to the transverse variable $z$. The degree of this polynomial is specified but does not have to be the same for all the components of the field. In general, each component is interpolated in the $z$ direction using a finite set of linearly independent functions as in the ansatz

$$w_{3D}(\mathbf{x}, z) = \sum_i w_i(\mathbf{x})\, v_i(z) \tag{38}$$

Across the thickness the field is interpolated with a set of shape functions $v_i$. Their coefficients $w_i$ vary depending on the position $\mathbf{x}$ of their projection on the middle-plate surface. Increasing the number of these functions (i.e. increasing the degree in the case of polynomials) yields a hierarchy of models of increasing order, whence the name of hierarchic plate theories [Babuska, Szabo, and Actis (1992)], in a very similar fashion to hierarchic finite elements [Zienkiewicz and Taylor (1989)]. The Kirchhoff-Love theory [Kirchhoff (1850, 1876); Love (1934)] represent the lowest level of this hierarchy, as the transverse displacement $w$ is kept constant across the thickness and the in-plane displacement is taken with a linear dependency on $z$. Additionally, it is necessary to satisfy the constraint that the coefficient of $z$ be the opposite of the gradient of $w$, expressing the geometrical statement that lines normal to the middle plane keep their orthogonality in the deformed state. The ansatz for the three-dimensional displacement is

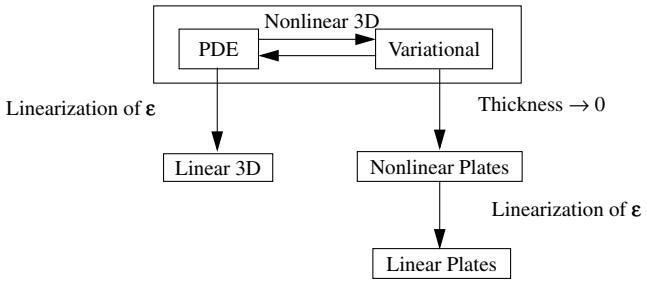


**Figure 1** : Hierarchy of models for elastodynamics.

$$\mathbf{u}_{3D} = \begin{bmatrix} \mathbf{u}(\mathbf{x}) - z\nabla w(\mathbf{x}) \\ w(\mathbf{x}) \end{bmatrix} \tag{39}$$

For Reissner-Mindlin plates, the through-thickness behavior is assumed as given by

$$\mathbf{u}_{3D} = \begin{bmatrix} \mathbf{u}(\mathbf{x}) - z\vartheta(\mathbf{x}) \\ w(\mathbf{x}) \end{bmatrix} \tag{40}$$

which differs from the Kirchhoff-Love [Reissner (1944, 1945, 1985); Mindlin (1951)] model in the independence of the z-coefficient on the in-plane displacement. The Reissner-Mindlin plate has received much attention because, contrary to Kirchhoff plate theory, $C^0$-continuity is sufficient to formulate finite element discretizations. This non-conforming approximation requires a reduced-order integration to retain proper flexibility for the plate. This means that instead of

using a Gaussian quadrature over the element, where the order of the quadrature is chosen to give exact results for the highest polynomial degree of the shape functions, a quadrature that guarantees exact results only for a lower polynomial degree is chosen, thus suppressing higher-order displacement behavior. Indeed, without uniform or selective reduced integration, elements incur "locking", a phenomenon in which the normal-integrated $C^0$-element fails to reproduce the Kirchhoff solution expected in the thin-plate limit. However, wider computing experience with the reduced-integration elements disclosed ill-conditioned behavior erratically dependent on element shapes and mesh patterns, an undesirable characteristic for elements intended for use in general-purpose software. Consequently a rich literature has flourished suggesting several methods to overcome these problems. On the other hand, the common place that the Reissner-Mindlin theory is "better" than the Kirchhoff-Love theory, is not yet fully substantiated [Ciarlet (1997)]. Therefore we took the decision to use the more sophisticated finite elements of class $C^1$ applied to the simpler Kirchhoff-Love theory, so as to achieve a conforming approximation, which is mathematically sounder and effects a higher degree of reliability of the simulated results.

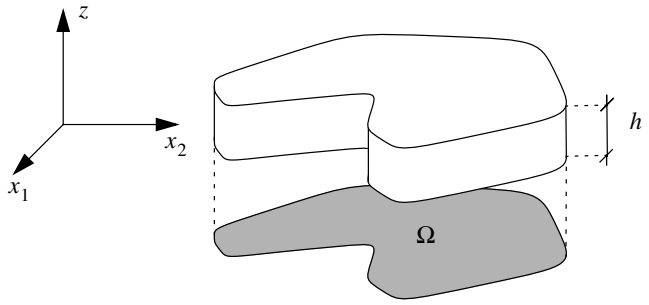


**Figure 2** : The three-dimensional geometry of a plate.

### *3.1 The 3D theory in the language of plates*

Describing the three-dimensional geometry of the plate as in Fig. 2

$$\Omega_{3D} = \Omega \times \left[-\frac{h}{2}, \frac{h}{2}\right] = \left\{ (\mathbf{x}, z) : \mathbf{x} \in \Omega, -\frac{h}{2} \leq z \leq \frac{h}{2} \right\} \tag{41}$$

the $L^2$ product for an arbitrary pair of fields $U$, $v$ on the solid plate is then decomposed as

$$(u, v)_{\Omega_{3D}} = \int_{-h/2}^{h/2} (u, v)_{\Omega} \, \mathrm{d}z \tag{42}$$

Henceforth the subscript $\Omega$ in the inner product and integration extrema $\pm h/2$ shall be omitted. The boundary of the solid plate is decomposed as

$$\partial\Omega_{3D} = \Omega \times \left\{ \frac{h}{2} \right\} + \Omega \times \left\{ \frac{h}{2} \right\} + \partial\Omega \times \left[-\frac{h}{2}, \frac{h}{2}\right] \tag{43}$$

i.e. into its perimeter wall, and its lower and upper planes. The boundary integral of a tensor A contracted with the normal is then expanded as

$$(n, A)_{\partial\Omega_{3D}} = \int_{\Omega} \left[\hat{\mathbf{z}} \cdot A\right]_0 \, \mathrm{d}\mathbf{x} + \left(n, \int A \, \mathrm{d}z\right)_{\partial\Omega}, \tag{44}$$

where the jump across $\Omega$ oriented along the normal to the plate is defined as

$$\left[A\right]_0 = A\left(\mathbf{x}, h/2\right) - A\left(\mathbf{x}, -h/2\right) \tag{45}$$

and its higher moments as

$$\left[A\right]_n = \left[z^n A\right]_0 = \left(\frac{h}{2}\right)^n \left[A\left(\mathbf{x}, h/2\right) - (-1)^n A\left(\mathbf{x}, -h/2\right)\right] \tag{46}$$

For any tensor field $A(\mathbf{x}, z)$ defined on the solid plate, its n-th order moment is defined as

$$A_n(\mathbf{x}) = \int z^n A(\mathbf{x}, z) \, \mathrm{d}z. \tag{47}$$

Using these definitions it is possible to rewrite the inertial virtual work as

$$\begin{aligned} W_I &= \left(\rho\ddot{\mathbf{u}}_{3D}, \delta\mathbf{u}_{3D}\right)_{\Omega_{3D}} \\ &= \left(\rho_0\ddot{\mathbf{u}} - \rho_1\nabla\ddot{w}, \delta\mathbf{u}\right) + \left(\rho_2\nabla\ddot{w} - \rho_1\ddot{\mathbf{u}}, \nabla\delta w\right) + \left(\rho_0\ddot{w}, \delta w\right) \end{aligned} \tag{48}$$

and that for a body force decomposed in its transverse and in-plane components as $f_{3D} = (f, g)$ the virtual work reads

$$\begin{aligned} W_B &= \left(f_{3D}, \delta\mathbf{u}_{3D}\right)_{\Omega_{3D}} \\ &= \left(f_0, \delta\mathbf{u}\right) - \left(f_1, \nabla\delta w\right) + \left(g_0, \delta w\right) \end{aligned} \tag{49}$$

According to Eq. 5, the (Green-St. Venant) three-dimensional strain is then

$$\varepsilon_{3D} = \begin{bmatrix} \varepsilon & \gamma/2 \\ \gamma^T/2 & \varepsilon_{33} \end{bmatrix} \tag{50}$$

with

$$\begin{aligned} \varepsilon &= \left(\nabla\mathbf{u}\right)^S + \left(\nabla w\right)\left(\nabla w\right)/2 - z\nabla\nabla w \\ &\quad + \left(\nabla\mathbf{u}\right)\cdot\left(\nabla\mathbf{u}\right)^T/2 - \left(z\nabla\nabla w\right)^2 \end{aligned} \tag{51}$$

$$\gamma = \left(\nabla\mathbf{u} - z\nabla\nabla w\right)\cdot\nabla w \tag{52}$$

$$\varepsilon_{33} = \left(\nabla w\right)^2 \tag{53}$$

### *3.2 Taking the plate limit*

In the limit case the in-plane strain reduces to

$$\varepsilon = \left(\nabla\mathbf{u}\right)^S + \left(\nabla w\right)\left(\nabla w\right)/2 - z\nabla\nabla w \tag{54}$$

which at the middle plane gives

$$\varepsilon_m = \left(\nabla\mathbf{u}\right)^S + \left(\nabla w\right)\left(\nabla w\right)/2 \tag{55}$$

The variation of the in-plane strain is

$$\delta\varepsilon = (\nabla\delta\mathbf{u})^S + (\nabla w)(\nabla\delta w) - z\nabla\nabla\delta w. \tag{56}$$

Imposing the additional condition of vanishing elastic reaction in the transverse direction, implies that only the in-plane components of the stress are different from zero

$$\sigma_{3D} = \begin{bmatrix} \sigma & 0 \\ 0 & 0 \end{bmatrix} \tag{57}$$

Thus, the elastic virtual work is

$$\begin{aligned} W_E &= (\sigma_{3D}, \delta\varepsilon_{3D})_{\Omega_{3D}} \\ &= \left(\sigma_0, (\nabla\delta\mathbf{u})^S\right) - (\sigma_1, \nabla\nabla\delta w) + (\nabla w\cdot\sigma_0, \nabla\delta w)_{\Omega\times T} \end{aligned} \tag{58}$$

which, by introducing the stress-strain relation, yields

$$\begin{aligned} W_E = &\left(A_0 : \varepsilon_m - A_1 : \nabla\nabla w + \sigma_0^{\text{ext}}, (\nabla\delta\mathbf{u})^S\right) \\ &- \left(A_1 : \varepsilon_m - A_2 : \nabla\nabla w + \sigma_1^{\text{ext}}, \nabla\nabla\delta w\right) \\ &+ \left(\nabla w\cdot\left(A_0 : \varepsilon_m - A_1 : \nabla\nabla w + \sigma_0^{\text{ext}}\right), \nabla\delta w\right) \end{aligned} \tag{59}$$

### *3.3 Linearization*

The virtual work of equation (Eq. 59) is non-linear. This means that the variational problem resulting by adding these terms to the other virtual works is non-linear. The linearization acts on the in-plane strain at the middle surface $\varepsilon_m$ and on the third row of equation (Eq. 59):

$$\begin{aligned} W_{E,\text{lin}} = &\left(A_0 : (\nabla\mathbf{u})^S - A_1 : \nabla\nabla w + \sigma_0^{\text{ext}}, (\nabla\delta\mathbf{u})^S\right) \\ &- \left(A_1 : (\nabla\mathbf{u})^S - A_2 : \nabla\nabla w + \sigma_1^{\text{ext}}, \nabla\nabla\delta w\right) \\ &+ \left(\nabla w\cdot\sigma_0^{\text{ext}}, \nabla\delta w\right) \end{aligned} \tag{60}$$

The resulting weak formulation for the mechanical plate is then given by the sum

$$W_I + W_E = W_B \tag{61}$$

Its linearity depends on the elastic virtual work $W_E$ only. Explicitly, the linearized virtual work is

$$\begin{aligned} &(\rho_0\ddot{\mathbf{u}} - \rho_1\nabla\ddot{w}, \delta\mathbf{u}) + (\rho_2\nabla\ddot{w} - \rho_1\ddot{\mathbf{u}}, \nabla\delta w) \\ &+ (\rho_0\ddot{w}, \delta w) + \left(\nabla w\cdot\sigma_0^{\text{ext}}, \nabla\delta w\right) \\ &+ \left(A_0 : (\nabla\mathbf{u})^S - A_1 : \nabla\nabla w + \sigma_0^{\text{ext}}, (\nabla\delta\mathbf{u})^S\right) \\ &- \left(A_1 : (\nabla\mathbf{u})^S - A_2 : \nabla\nabla w + \sigma_1^{\text{ext}}, \nabla\nabla\delta w\right) \\ &= (f_0, \delta\mathbf{u}) - (f_1, \nabla\delta w) + (g_0, \delta w) \end{aligned} \tag{62}$$

The equation is discretized using finite elements by interpolating the fields $\mathbf{u}$ and $w$ with a set of shape functions, and using each of these shape functions as the test functions $\delta\mathbf{u}$ and $\delta w$. For the in-plane displacement (for the transverse displacement a similar relation holds) the unknown field is interpolated as

$$\mathbf{u}(t, \mathbf{x}) = \sum_i \mathbf{u}_i(t) N_i(\mathbf{x}) \tag{63}$$

An approximation is conforming if the approximating function is in the same space as the approximated field, non-conforming in the other case [Bernadou (1996)]. Inspecting equation (Eq. 62) shows that because of the term

$$(A_2 : \nabla\nabla w, \nabla\nabla\delta w) \tag{64}$$

the transverse displacement requires that also second derivatives must be square integrable, i.e. $w \in H^2(\Omega)$, so that, in order to have a conforming discretization, the shape functions must be elements of $H^2(\Omega)$. The Sobolev embedding theorem then states that the shape functions must be of class $C^1(\Omega)$. This can be achieved implementing the Argyris element of Fig. 3.

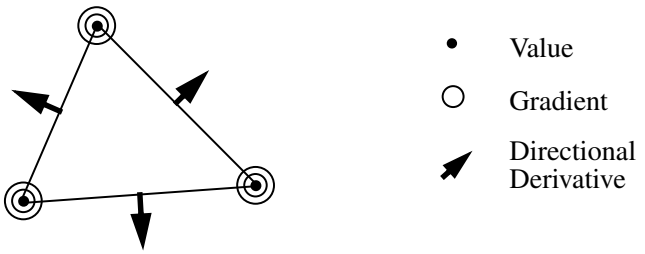


**Figure 3** : The Argyris Element [Argyris, Fried, and Scharpf (1968)].

## 4 Fluctuations and noise

The excitation of a vibration response in a micro-beam is created by coupling the various degrees of freedom of the gas-system to a set of linear harmonic oscillators, that are formed by the spectrum of the vibrational structure. This description holds for a wide range of cases. The governing fluctuating process at room temperature changes with the gas density, the scattering rate for molecules impinging on the cantilever surface growing with the density. Thus, the scattering rates of the impinging gas-molecules are by orders of magnitude larger than those stemming from the coupling with phonons or other elementary excitations. The coupling clearly depends on the mode spectrum of the respective degree of freedom. For a cantilever of length $100\,\mu$m and a quadratic cross section of $1\,\mu$m by $1\,\mu$m the transition regime of the gas pressure for the transverse vibration-modes is of the order of $10^{-5}$ bar [Yasamura, Stowe, Chow, Pfafman, Kenny, and Rugar (1998)].

All beam-modes have the same thermal energy. Each mode's mean square amplitude is completely determined by the ambient temperature. According to the equipartition theorem,

each mode carries the thermal energy $k_B T$, where $T$ is the temperature and $k_B$ the Boltzmann constant, just as any kinetic degree of freedom of the gas molecules. Thus, the mean square vibration-amplitude of the beam does not depend on the ambient pressure. Differences between various environmental conditions affect only the temporal behavior of the randomly vibrating cantilever, and in particular the tempral correlation functions of the mode amplitudes. Therefore, these show significant changes under different pressure conditions for a gaseous environment, thus characterizing the system and the coupling to its environment. The calculation of the correlation function by means of simulations is the subject of the following sections.

### *4.1 Vibration modes of a micro-cantilever*

To calculate the correlation function of the mode amplitudes for a vibrating cantilever we first have to determine the vibration mode functions. For very simple geometries this can be done analytically, while for complex structures numerical methods have to be applied. We consider a cantilever of length $l$ along the $x$-direction clamped at $x = 0$ and free at the other end. Its cross section is rectangular with height $h$ and width $b$. We restrict the discussion to the transverse vibration of a bar with rectangular cross section [Butt and Jaschke (1995)]. The equation of motion for the transverse displacement field $u$ for the case of a thin and long (slender) bar is given by [Landau and Lifshitz (1986)]

$$\frac{\partial^2 u(x,t)}{\partial t^2} + \frac{Eh^2}{12\rho}\frac{\partial^4 u(x,t)}{\partial x^4} = 0, \tag{65}$$

where $E$ is the elastic modulus of the bar material and $\rho$ is its density. Together with the boundary conditions

$$u|_{x=0} = \left.\frac{\partial u}{\partial x}\right|_{x=0} = \left.\frac{\partial^2 u}{\partial x^2}\right|_{x=l} = \left.\frac{\partial^3 u}{\partial x^3}\right|_{x=l} = 0 \tag{66}$$

this results in an eigenvalue problem for which the complete time response is given by a superposition of eigenvectors with a harmonic time dependence

$$u(x,t) = \sum_j \xi_j \sin(\omega_j t + \theta_j)\, w_j(x) \tag{67}$$

The vibrational modes $w_j(x)$ are given by

$$\begin{aligned} w_j(x) = {} & [\sin(k_j l) + \sinh(k_j l)]\,[\cos(k_j x) - \cosh(k_j x)] \\ & - [\cos(k_j l) + \cosh(k_j l)]\,[\sin(k_j x) - \sinh(k_j x)] \end{aligned} \tag{68}$$

The vibration frequencies $\omega_j$ read

$$\omega_j = \sqrt{\frac{Eh^2 k_j^4}{12\rho}} \tag{69}$$

where the wave vectors $k_j$ must satisfy for the case of a clamped-free beam considered here the condition

$$\cos(k_j l)\cosh(k_j l) = -1 \tag{70}$$

The energy of the transverse vibration modes is given by

$$W = \frac{Ebh^3}{24}\int_0^l \left[\frac{\partial^2 u(x,t)}{\partial x^2}\right]^2 \mathrm{d}x + \frac{\rho bh}{2}\int_0^l \left[\frac{\partial u(x,t)}{\partial t}\right]^2 \mathrm{d}x \tag{71}$$

Inserting the superposition solution (Eq. 67) and using the orthogonality of the eigenvectors $w_j$ (and of their second derivatives) yields the total vibrational energy [Butt and Jaschke (1995)]

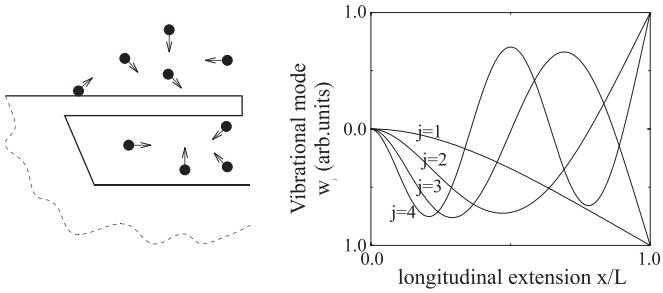


(a) (b)

**Figure 4** : a) Gas molecules impinging on the micro-bar, b) first four vibrational mode functions. The longitudinal extension is normalized to the length $L$ of the bar.

$$\begin{aligned} W = {} & \frac{K}{2}\sum_{j=0}^{\infty} \xi_j^2 (k_j l)^4 \sin^2(\omega_j t + \theta_j)\,\frac{I_j}{3} \\ & + \frac{1}{2M}\sum_{j=0}^{\infty} \xi_j^2 (M\omega_j)^2 \cos^2(\omega_j t + \theta_j)\, I_j \end{aligned} \tag{72}$$

where $M$ is the total cantilever mass and the spring constant $K$ is given by

$$K = \frac{Ebh^3}{4l^3}. \tag{73}$$

The mean square displacement per mode is given by

$$I_j = \frac{1}{l}\int_0^l w_j^2 \mathrm{d}x. \tag{74}$$

From Eq. 72 we see that the linear vibrating bar may be described as an ensemble of non-interacting, i.e. decoupled, harmonic oscillators. Note that this holds for arbitrary linear vibrating structures. Rewriting the total energy in terms of the modal amplitudes and momenta

$$q_j(t) = \xi_j \sin(\omega_j t + \theta_j) \tag{75}$$

$$p_j(t) = M\omega_j \xi_j \cos(\omega_j t + \theta_j) \tag{76}$$

yields

$$W = \frac{K}{2}\sum_{j=0}^{\infty} q_j^2(t)\,\frac{(k_j l)^4 I_j}{3} + \frac{1}{2M}\sum_{j=0}^{\infty} p_j^2(t)\, I_j \tag{77}$$

For a harmonic oscillator with a quadratic form of the total energy as given in Eq. 77 we know that the equipartition theorem holds. Therefore, a mean square vibration amplitude results from the interaction with the gas molecules impinging on the micro-bar as schematically shown in Fig. 4a.

### 4.2 Correlation functions of vibrational mode-amplitudes

The thermal motion of the gas molecules is completely random and uncorrelated. The oscillator modes are well defined for a given frequency $\omega_j$ and wave vector $k_j$ as shown in Fig. 4b. The continuous impinging of molecules on the cantilever surface results in a random momentum transfer from the gas to the cantilever and vice versa. Eventually this process yields a mean square amplitude per mode of the form [Butt and Jaschke (1995)]

$$\left\langle q_j^2 \right\rangle = \frac{3k_BT}{(k_j l)^4 KI_j} \tag{78}$$

which, remarkably, is independent from the species of the gas molecules. The number of impacts per unit surface area and per unit time interval is given by [Reif (1965)]

$$r = \frac{N}{V}\sqrt{\frac{k_BT}{2\pi m}} = \sqrt{\frac{P}{2\pi m k_BT}} \tag{79}$$

where $N/V$ is the number density of gas molecules, $T$ is the temperature, $m$ is the mass of a gas molecule and $P$ the pressure of the gas. This tells us that there is a significant dependence on the specific gas to be reflected in the dynamics of the amplitude $q_j(t)$. To illustrate this fact we derive the equations of motion for a single mode from Eq. 72

$$\dot{q}_j = \frac{I_j}{M}p \tag{80}$$

$$\dot{p}_j = -I_j M\omega_j^2 q + \Delta p(t)\,. \tag{81}$$

Here $\Delta p(t)$ is a random function that results in a completely uncorrelated noise source and a damping caused by the impinging molecules. For the average momentum transfer,

$$\langle \Delta p(t) \rangle = 0 \tag{82}$$

holds. The resulting random momentum transfer per unit time interval is $\Delta p = 2\sqrt{mk_BT}$, which is roughly twice the average momentum per molecule perpendicular to the cantilever surface. This is a coarse-grained picture for the microscopic processes. The distribution function of the molecules is taken to be Maxwellian in momentum space and uniform in position space.

### 4.3 Simulation procedure

In order to calculate the fluctuations in the vibrational mode amplitudes in a realistic environment the molecules are assumed to follow a Maxwellian distribution. Consider the fundamental transverse vibration mode ($j = 1$, see Fig. 4a and b). In order to perform a simple Euler-forward integration of Eq. 81, we have to determine the momentum transfer on the cantilever-mode for each time-step. This requires a series of random numbers, since Eq. 79 only provides us with the total number of molecules impinging on the unit area in a unit time interval. Taking the normal pressure of $P = 1\,\mathrm{bar}$ and a temperature $T = 300\,\mathrm{K}$ of an air-like gas with molecular mass of roughly $m = 30\,\mathrm{amu}$ ($1\,\mathrm{amu} = 1.66 \times 10^{-14}\,\mathrm{g}$, the atomic mass unit) we get an impinging rate per unit area of $r = 9 \times 10^{24}\,\mathrm{s^{-1}m^{-2}}$. This quantity has to be multiplied by the surface area $A$ of the cantilever that couples momentum into the respective mode, which in our case is $A = 2 \times 10^{-10}\,\mathrm{m^2}$. This yields a scattering-rate $r_{sc} = 9 \times 10^{14}\,\mathrm{s^{-1}}$, which means that, under the described normal conditions, a molecule hits the active surface every 100 fs. The fact that molecules are scattered from both faces of the active area means that the average momentum transfer has both signs, negative and positive, such that in a long time average the force acting on the micro-cantilever is zero. We choose a time interval $\Delta t = r_{sc}^{-1}$ with one particle impinging on $A$. The first of the two random numbers needed at every step is used to decide whether there is a momentum transfer from the gas to the cantilever in the time interval $\Delta t$. Because of the homogeneity of the gas, the azimutal angles and the polar angles of an impinging molecules are uniformly distributed. The polar angle with respect to the active area has no significance, while the cosine of the azimutal angle is the determining factor once the linear momentum of the impinging molecule is known. This linear momentum follows the Maxwellian distribution for the velocities of the gas molecules. The second random number determines the value of a component of their momenta normal to the surface of the cantilever.

The mode amplitude is given by

$$\xi = \sqrt{\frac{\omega^2 m}{2}q^2 + \frac{1}{2m}p^2} \tag{83}$$

The correlation function $C(\tau)$ of the deviation of the mode amplitudes $\xi$ from its average value $\langle\xi\rangle$ is given by $C(\tau) = \langle \Delta\xi(t)\,\Delta\xi(t+\tau)\rangle$ with $\Delta\xi(t) = \xi(t) - \langle\xi\rangle$. We now describe the dynamics of $\Delta\xi(t)$ by a Langevin equation of the form [Lax (1960)]

$$\frac{\mathrm{d}\Delta\xi(t)}{\mathrm{dt}} = -\gamma\Delta\xi(t) + F(t) \tag{84}$$

where $\gamma$ is the damping constant and F(t) is the fluctuating force for which

$$\langle F(t)\rangle = 0 \tag{85}$$

$$\left\langle F(t)\,F\left(t'\right)\right\rangle = 2D\delta\left(t - t'\right) \tag{86}$$

must hold [Lax (1960)]. Thus it can be shown [Reif (1965)] that

$$C(\tau) = \langle \Delta\xi(t)\,\Delta\xi(t+\tau)\rangle = \langle \Delta\xi(0)\,\Delta\xi(0)\rangle \exp(-\tau\gamma)\,. \tag{87}$$

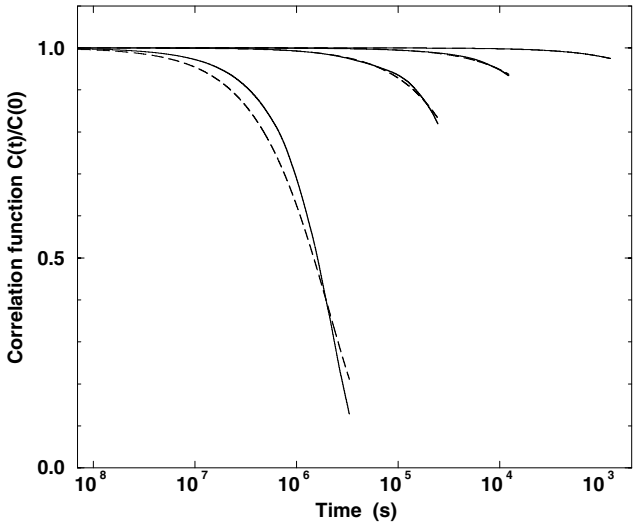


**Figure 5** : Correlation functions of the vibrational amplitudes of the first mode for 4 different gas densities $(10^{-4}, 10^{-5}, 10^{-6}, 10^{-7}\mathrm{kg\,m^{-3}})$. The simulated gas environment was at $T = 300\,\mathrm{K}$ and the molecular mass was 30 amu. The bar geometry was taken as $l = 100\,\mu\mathrm{m}$, $h = 1\,\mu\mathrm{m}$, $b = 1\,\mu\mathrm{m}$, and its density was $10^3\mathrm{kg\,m^{-3}}$ while the elastic modulus was taken as $E = 100\,\mathrm{GPa}$. The solid lines show the calculated correlation functions and the dotted lines are exponential fits according to Eq. 87.

Eq. 87 induces a natural way of extracting the damping constant $\gamma$ from the microscopic simulations. It is sufficient to extract the variance $C(0) = \langle \Delta\xi(0)\,\Delta\xi(0)\rangle$ and the initial slope of $C(\tau)$ in order to have the exponential functions fitted as shown in Fig. 5. This procedure is necessary because we do not know the fluctuating forces of a corresponding Langevin type behavior.

## 5 Mesh adaptivity

Two decades have passed since self-adaptive finite element discretization methods were introduced into the engineering literature [Zienkiewicz and Zhu (1987)]. They have gained increasing importance for the numerical solution of partial differential equations which arise from engineering applications.

The general idea is to obtain a numerical solution within a prescribed tolerance for a minimum of effort expressed in terms of storage capabilities and computational time needed by the computing device at hand. The main tools are: a posteriori error estimators which give global and local information on the error of the numerical solution; refinement strategies, used in order to decide which regions have to be refined. The strategies are usually based on an evaluation of local error information. To complete the scheme, a geometric method is needed which specifies aspects of how a given region has to be refined.

For parabolic problems the theory is not as developed as for elliptic problems, and for hyperbolic problems the field is still in its infancy [Verfürth (1996)]. Here we present a number of tools most frequently used for the adaptive finite element method. The ideas have been under constant development by various authors over the last 20 years.

One of the difficulties often encountered while solving practical engineering problems (e.g. computational fluid dynamics, elasticity, or semiconductor device simulation) is that the overall accuracy of the numerical approximation is deteriorated by local singularities, caused, for example, by re-entrant corners. Intuitively, a selective measure would be to refine the discretization near critical regions by adding grid points to regions where the solution is less regular. The question is then how to identify these regions and how to keep a good balance between refined and unrefined regions such that the overall accuracy is optimal.

In general, the only data available to the analyst providing useful indication of the error is the approximate solution itself. Therefore, the challenge is to obtain an a posteriori estimate of the error, i.e. following the initial approximate solution, under the constraint that the calculation of the estimate should be far less expensive than the computation of the numerical solution. Moreover, the error estimator should be local and should yield reliable upper and lower bounds for the error in a suitable norm. Such bounds ensure that the actual error and the error estimate decrease at the same rate when the mesh is refined. In particular, it can be proved that if an adaptive procedure is implemented that reduces the error estimate then the error itself is also decreased, and at the same rate as the estimate.

In conjunction with an a posteriori error estimator, an adaptive mesh-refinement process has the following general structure [Verfürth (1996)]:

1. Construct an initial coarse mesh $S_0$ of finite elements representing sufficiently well the geometry of the problem. Set the iteration counter $k = 0$.
2. Solve the discrete problem on $S_k$.
3. For each finite element S in $S_k$ compute an a posteriori error estimate.
4. If the estimated global error is sufficiently small then stop. Otherwise decide which elements have to be refined and construct the next mesh $S_{k+1}$. Increment the counter $k$ and return to step 2.

This is the algorithm usually applied for stationary problems. It has to be modified in case we deal with transient calculations:

1. Estimate the accuracy of the computed numerical solution every few time steps.
2. Couple the refinement process in space with a time step size control.

3. Partially coarsen the mesh if necessary.
4. Occasionally, a complete re-meshing could be desirable.

In both stationary and transient problems the refinement process might be coupled with a moving point technique, which keeps the number of grid points constant but changes their relative location [Ribbens (1989)].

### 5.1 A posteriori error estimates

There are in general several classes of methods with which to obtain an a posteriori error estimate suitable for use with adaptive finite element methods. We review the first one for a model problem in the next sections [Babuska and Reinboldt (1978); Babuska, Zienkiewicz, Gago, and de A. Oliveira (1986); Bank and Weiser (1985); Verfürth (1996)].

(1) residual estimates: Estimate the error of the computed numerical solution by a suitable norm of its residual with respect to the strong form of the differential equation.

(2) solution of local problems: Solve locally discrete problems similar to, but simpler than the original problem and use appropriate norms of the local solutions for error estimation.

(3) hierarchical basis error estimates: Evaluate the residual of the computed finite element solution with respect to another finite element space corresponding to higher order elements or to a refined grid.

(4) averaging methods: Use some local extrapolation or averaging technique for error estimation. It has been shown that all these techniques rely on a common principle: the error of the computed finite element approximation may be represented as a residual in the dual of an appropriate Banach space. The norm of this residual must be calculated in a sufficiently accurate and efficient way [Verfürth (1996)].

### 5.2 The model problem and its discretization

As a model problem we consider the two-dimensional Poisson partial differential equation (PDE) with mixed Dirichlet-Neumann boundary conditions (BCs) [Verfürth (1996)]

$$-\Delta u = f \qquad \text{in } \Omega \qquad \text{(The PDE)} \tag{88}$$

$$u = 0 \qquad \text{on } \Gamma_D \qquad \text{(The Dirichlet BC)} \tag{89}$$

$$\frac{\partial u}{\partial n} = g \qquad \text{on } \Gamma_N \qquad \text{(The Neumann BC)} \tag{90}$$

in a connected, bounded, polygonal domain $\Omega \subset \mathbb{R}^2$ with boundary $\partial\Omega = \Gamma_D \cup \Gamma_N$, $\Gamma_D \cap \Gamma_N = \emptyset$. We assume that $\Gamma_D$ is closed relative to $\partial\Omega$ with non-null length and that $f$ and $g$ are square integrable functions respectively on $\Omega$ and $\Gamma_N$. For any open subset $\bar{\Omega}$ of $\Omega$ with Lipschitz boundary $\partial\bar{\Omega}$ (i.e., physically plausible) we denote by $L^2(\bar{\Omega})$, and $H^1(\bar{\Omega})$ the standard Lebesgue and Sobolev-spaces equipped with the usual norms

$$\|\varphi\|_{0,\bar{\Omega}} = \left\{ \int_{\bar{\Omega}} \varphi^2 \right\}^{1/2} \tag{91}$$

and

$$\|\varphi\|_{1,\bar{\Omega}} = \left\{ \int_{\bar{\Omega}} \left( \varphi^2 + |\nabla\varphi|^2 \right) \right\}^{1/2} \tag{92}$$

In order to have a more compact notation, throughout this section the integration variables and measures are omitted. Integrations over $\Omega$ are intended with the measure $\mathrm{d}^2x$ and those on $\Gamma_N$, $\Gamma_D$ with $l(\mathbf{x})$. If $\bar{\Omega} = \Omega$, we omit the index $\bar{\Omega}$. We now set the space of approximation functions $X$ as

$$X := \left\{ \varphi \in H^1(\Omega) : \varphi = 0 \text{ on } \Gamma_D \right\} \tag{93}$$

The weak formulation of Problem (88–90) is then finding $u \in X$ such that

$$\int_\Omega \nabla u \cdot \nabla s = \int_\Omega fs + \int_{\Gamma_N} gs \qquad \forall s \in X \tag{94}$$

which admits a unique solution. For a triangulation $T_h$ of $\Omega$ such that any pair of triangles share at most a common edge or vertex and the angles of all triangles are bounded from below, it is possible to define a finite element discretization of equation (5): Find $u_h \in X_h$ such that

$$\int_\Omega \nabla u_h \cdot \nabla s_h = \int_\Omega fs_h + \int_{\Gamma_N} gs_h \qquad \forall s_h \in X_h \tag{95}$$

where $X_h$ denotes the space of all continuous, piecewise linear finite element functions corresponding to the triangulation and vanishing on $\Gamma_D$. It is well known that also Eq. 95 admits a unique solution. In order to keep the notational and technical apparatus at a minimum we restrict ourselves to linear finite elements. We end this section by introducing additional notations which will be needed for constructing and analyzing the error estimators in the next section. For any triangle $T \in T_h$, the set of its edges are denoted by $E(T)$. The set of all the edges in the triangulation

$$E_h := \bigcup_{T \in T_h} E(T) \tag{96}$$

is partitioned as

$$E_h = E_{h,\Omega} \cup E_{h,D} \cup E_{h,N} \tag{97}$$

where $E_{h,\Omega}$, $E_{h,D}$ and $E_{h,N}$ indicate the edges in the interior of $\Omega$, on $\Gamma_D$ and on $\Gamma_N$, respectively.

### 5.3 A residual error estimator

Let $u \in X$ and $u_h \in X_h$ be the exact solutions of Eq. 94 and Eq. 95. They satisfy the identity

$$\int_\Omega \nabla(u - u_h) \cdot \nabla s = \int_\Omega fs + \int_{\Gamma_N} gs - \int_\Omega \nabla u_h \cdot \nabla s \qquad \forall s \in X \tag{98}$$

The right hand side of Eq. 98 implicitly defines the residual of $u_h$ as an element of the dual space of X. Since $\Gamma_D$ has positive length, a Poincaré-Friedrichs inequality holds

$$\|s\|_1 \leq c_\Omega \|\nabla s\|_0 \qquad \forall s \in X \tag{99}$$

The constant $c_\Omega$ depends only on $\Omega$ and on the length of the Dirichlet-boundary. Inequality (Eq. 99) and the Cauchy-Schwarz inequality then imply for all $s \in X$, $\|w\|_1 = 1$

$$\left(\frac{1}{1+c_\Omega^2}\right)\|s\|_1 \leq \sup_{w\in X}\int_\Omega \nabla s\cdot\nabla w \leq \|s\|_1 \tag{100}$$

Eq. 98 and Inequality (Eq. 100) imply the estimate

$$\begin{aligned}\sup_{w\in X}\left(\int_\Omega fw+\int_{\Gamma_N} gw-\int_\Omega \nabla s\cdot\nabla w\right) &\leq \|u-u_h\|_1 \\ &\leq \left(1+c_\Omega^2\right)\cdot\sup_{w\in X}\left(\int_\Omega fw+\int_{\Gamma_N} gw-\int_\Omega \nabla s\cdot\nabla w\right)\end{aligned} \tag{101}$$

Evaluating the sup-term in inequality (Eq. 101), observing that the error is orthogonal to $X_h$ and applying Clément's Approximation Theorem gives the following estimate

$$\begin{aligned}\frac{1}{c^2}\|u-u_h\|_1^2 \leq &\sum_{T\in T_h} h_T^2\cdot\|f\|_{0,T}^2+\sum_{E\in E_{h,N}} h_E\cdot\|g-n_E\cdot\nabla u_h\|_{0,E}^2 \\ &+\sum_{E\in E_{h,\Omega}} h_E\cdot\|\lceil n_E\cdot\nabla u_h\rceil\|_{0,E}^2\end{aligned} \tag{102}$$

where the constant c essentially depends on the smallest angle of the triangulation and $h_T$ and $h_E$ are the corresponding diameters. The first sum on the right-hand side considers the approximation error caused by the "driving force" $f$ in the element interiors, whereas the second sum describes an error which is introduced by the deviation of the approximated from the prescribed normal flux on the boundary. The last term on the right-hand side considers the jumps of the gradient along a given edge in the domain interior ($n_E$ denotes the element edge's outward normal). Defining, for triangles and edges, the averages

$$f_T = \frac{1}{|T|}\int_T f(x) \tag{103}$$

$$g_E = \frac{1}{h_E}\int_E g(x) \tag{104}$$

finally yields a local error estimator only involving data known from the geometry and a computed solution

$$\begin{aligned}\left(\frac{\eta_{R,T}}{c}\right)^2 = &h_T^2\cdot\|f_T\|_{0,T}^2+\sum_{E\in E_{h,N}\cap E(T)} h_E\cdot\|g_E-n_E\cdot\nabla u_h\|_{0,E}^2 \\ &+\frac{1}{2}\sum_{E\in E_{h,\Omega}\cap E(T)} h_E\cdot\|\lceil n_E\cdot\nabla u_h\rceil\|_{0,E}^2\end{aligned} \tag{105}$$

Having deduced a reliable error estimator we now can continue our search for a decision on which elements must be refined or eventually be coarsened.

### *5.4 Refinement strategy*

From heuristic arguments we know that among all partitions of a linear finite element discretization, that one is optimal which equilibrates the error. I.e., the errors in all elements should be made equal. Among others, the most popular realization is called the maximum strategy and is done in the following way [Verfürth (1996)]: Suppose that for a given mesh a solution and an error estimator $\eta_T$ for each element has been computed. Let $\eta = \max_{T\in T_h}\eta_T$ and split an element $T$ if $\eta_T \geq \zeta\eta$ where $\zeta$ is a prescribed threshold, $0 < \zeta < 1$. This strategy, applied iteratively, would continue indefinitely. A halting condition is simple to add: stop if $\eta \leq \eta_{\text{accept}}$.

### *5.5 Split patterns*

The way in which the refinement process is performed, from a geometrical point of view, depends on the kind of elements present in the mesh. Difficulties arise from keeping shape regularity and from handling hanging nodes. Many rules have been established for the splitting of simplicial mesh constituents, such as e.g. the "red","green" or "blue" refinement for triangles.

We review a recursive algorithm for triangles which is based on the longest edge bisection. It has been shown that only a finite number of different angles occur during the refinement process and therefore shape regularity is guaranteed [Bänsch (1991), Rivara (1984), Rosenberg and Stenger (1975)]:

```
recursiveRefine(triangle_element):
begin
    repeat
        if neighbor has non-compatible
            refinement-edge
        then recursiveRefine(neighbor);
    until neighbor has compatible
        refinement-edge;
    bisect both triangles at the refinement-edge;
end
```

Compatibility is given if the neighbor element's longest edge is at the same time the longest edge of the target element or is a part of the boundary. The terminating recursive algorithm modifies the vicinity of the target element until its edge can be split (see Fig. 6).

## 6 Results: the AFM beam

The Kirchoff-Love-Argyris finite element has been implemented in our software environment for microsystem simulation [Emmenegger, Taschini, Korvink, and Baltes (1998), Emmenegger, Korvink, Bächtold, von Arx, Paul, and Baltes (1998)]. When applied to a clamped-clamped beam using 20 triangular finite elements, the solution of the eigenproblem yields mode shapes and frequencies matching the analytical solution within 1% up to the ninth mode. Subsequently

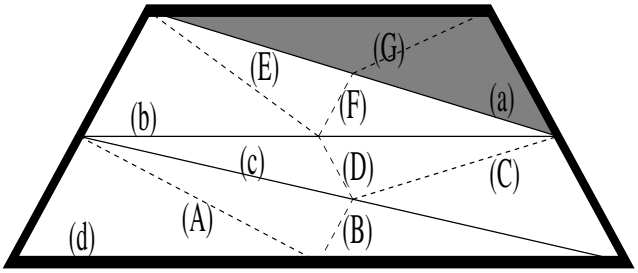


**Figure 6** : An elementary mesh consisting of 4 triangles from which the shaded one is marked to be split along edge (a). The dashed lines show how the recursive bisectioning algorithm produces new triangles, continuing down the geometry until the first edge (d) can be split, then backtracking to (c), (b) and finally (a). The capital letters label the order in which new edges are introduced on the return path of the recursive algorithm (depth 4).

we used the elements to determine the first six free vibration modes and their associated resonance frequencies for a CMOS AFM beam (Fig. 7]) [Lange, Akiyama, Hagleitner, Tonin, Hidber, Niedermann, Staufer, de Rooij, Brand, and Baltes (1999)].

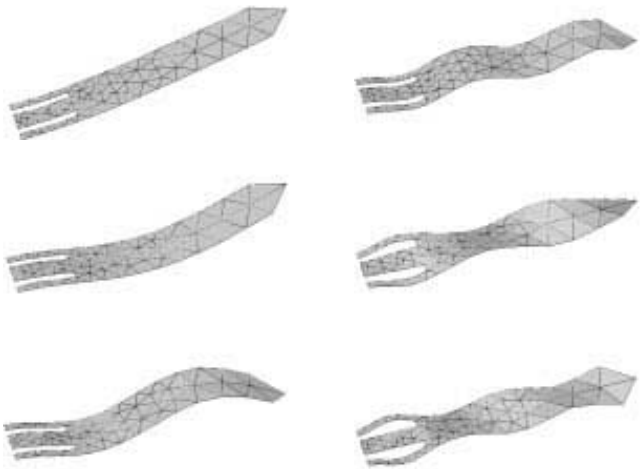

**Figure 7** : Vibrational modes of a micromachined CMOS AFM beam.

Thermal analysis of the AFM beam allows us to demonstrate the adaptive refinement process in a straightforward manner. We therefore compute the solution to Poisson's equation (the heat equation). Fig. 8 shows the mesh after the 8th refinement step where the error for a starting coarse mesh was reduced by a factor of around five. We clearly see that the refinement is deeper in regions close to singularities which arise from reentrant corners.

The decay of the correlation functions as shown in Fig. 5 must be explained by the complete randomization of the oscillator phase due to the impinging molecules. The momentum transfer is taken as an instantaneous scattering process between the gas molecule and the momentum of the vibrating bar. Thus it enters only the momentum equation of the micro-bar [Lax (1960)]. The higher the atmospheric pressure gets the faster the correlation decays. This yields a damping of the vibrational mode which has been observed by Yasamura, Stowe, Chow, Pfafman, Kenny, and Rugar (1998). If more complicated scattering processes are present the correlation function will show more structure. The setup in Fig. 5 shows well separated time-scales between the molecular dynamics and the vibrational angular frequency of about 1MHz. The scattering rate of the molecules with the micro-bar is 6 orders of magnitude higher. The noise behavior may be determined by investigating the correlation functions of observable quantities, taking into account different scattering processes [Greiner and Korvink (1998)]. An exponential decay of the correlation function stands for a single dominant process resulting in a single time-scale. The structure in fluctuating forces thus must be reflected in the correlation function of mode amplitude taken as a random variable.

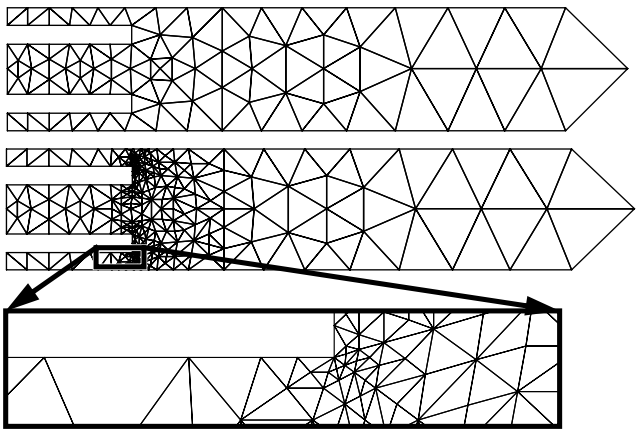

**Figure 8** : Adaptive refinement for a mixed Neumann-Dirichlet BVP for heat transfer.

## 7 Summary

Computing the dynamic response of thermomechanical microstructures requires a discretization scheme that enables accurate numerical solutions on coarse unstructured grids. Ideally, the grids may come from mesh generators that disregard subsequent computational steps, so that no guarantee on mesh quality may be assumed. Accuracy is obtained by subsequent mesh refinement. In addition, mesh refinement is so constrained to ensure that the mesh quality keeps on improving as well.

An adaptive refinement scheme is indispensable to achieve the high computational accuracy needed for microsystem applications. During the last two decades a posteriori error analysis has been well developed for elliptical problems. Since the complexity of simulation problems increases with computational resources, theoretical and technical approaches have to be combined in a sophisticated way and tailored to real world applications. Future work will concentrate on an extension of error analysis to parabolic and hyperbolic problems and by the demand for faster, more accurate and more reliable microsystem simulation code. This can only be met by a combined effort of numerical analysis, computer science and microsystem design.

With the aid of accurate noise predictions for real geometries we will concentrate on the extraction of compact model damping parameters and geometrical design rules.

**References**

**Argyris, J. H.; Fried, I.; Scharpf, D. W.** (1968): The TUBA family of plate elements for the matrix displacement method. *Aero. J. Royal Aeronaut. Soc.*, vol. 72, pp. 701–709.

**Ashcroft, N. W.; Mermin, N. D.** (1976): *Solid state physics*. Holt Rinehart and Winston, New York.

**Babuska, I.; Reinboldt, W.** (1978): Error estimates for adaptive finite element computations. *SIAM J. Numer. Anal.*, vol. 15, pp. 736–754.

**Babuska, I.; Szabo, B. A.; Actis, R.** (1992): Hierarchic models for laminated composites. *Internat. J. Numer. Methods Engrg.*, vol. 33, pp. 503–536.

**Babuska, I.; Zienkiewicz, O. C.; Gago, J.; de A. Oliveira, E. R.**(Eds): *Accuracy estimates and adaptive refinements in finite element computations*. Wiley, New York.

**Bank, R. E.; Weiser, A.** (1985): Some a posteriori error estimators for elliptic partial differential equations. *Math. Comput.*, vol. 44, pp. 283–301.

**Bänsch, E.** (1991): Local mesh refinement in two and three dimensions. *Impact Comp. Sc. Engrg*, vol. 3, pp. 181–191.

**Bernadou, M.** (1996): *Finite element methods for thin shell problems*. John Wiley & Sons, Chichester.

**Butt, H.-J.; Jaschke, M.** (1995): Calculation of thermal noise in atomic force microscopy. *Nanotechnology*, vol. 6, no. 1.

**Ciarlet, P. G.** (1997): *Mathematical elasticity, Vol II: Theory of plates*. North Holland.

**Emmenegger, M.; Korvink, J. G.; Bächtold, M.; von Arx, M.; Paul, O.; Baltes, H.** (1998): Application of harmonic finite element analysis to a CMOS heat-capacity measurement structure. *Sensors and Materials*, vol. 10, pp. 405–412.

**Emmenegger, M.; Taschini, S.; Korvink, J. G.; Baltes, H.** (1998): Simulation of a thermomechanically actuated gas sensor. In *Proc. IEEE MEMS*, pp. 184–189, Heidelberg.

**Gibbs, J. W.; Wilson, E. B.** (1901): *Vector analysis*. Yale University Press.

**Greiner, A.; Korvink, J. G.** (1998): Extraction of noise parameters for the macromodelling of MEMS. In *ASDAM '98*, Smolenice Castle, Slovakia.

**Kirchhoff, G.** (1850): Über das Gleichgewicht und die Bewegung einer elastischen Scheibe. *J. Reine Angew. Math.*, vol. 40.

**Kirchhoff, G.** (1876): *Vorlesungen über mathematische Physik*. Mechanik, Leipzig.

**Landau, L. D.; Lifshitz, E. M.** (1986): *Theory of elasticity*. Pergamon, Oxford.

**Lange, D.; Akiyama, T.; Hagleitner, C.; Tonin, A.; Hidber, H. R.; Niedermann, P.; Staufer, U.; de Rooij, N. F.; Brand, O.; Baltes, H.** (1999): Parallel scanning AFM with on-chip circuitry in CMOS technology. In *Proc. IEEE MEMS*, pp. 447–453, Orlando.

**Lax, M.** (1960): Fluctuations from the nonequilibrium steady state. *Rev. Mod. Phys.*, vol. 32, no. 25.

**Love, A. E. H.** (1934): *The mathematical theory of elasticity*. Cambridge University Press.

**Mindlin, R. D.** (1951): Influence of rotatory inertia and shear on flexural motions of isotropic elastic plates. *J. Appl. Mech.*, vol. 18, pp. 31–38.

**Nathan, A.; Baltes, H.** (1999): *Microtransducer CAD*. Springer-Verlag.

**Nye, J. F.** (1985): *Physical properties of crystals*. Oxford University Press.

**Reif, F.** (1965): *Fundamentals of statistical and thermal physics*. MacGraw-Hill Book Company.

**Reissner, E.** (1944): On the theory of bending of elastic plates. *J. Math. Phys.*, vol. 23, pp. 184–191.

**Reissner, E.** (1945): The effect of transverse shear deformations on the bending of elastic plates. *J. Appl. Mech.*, vol. 12, pp. A69–A77.

**Reissner, E.** (1985): Reflections on the theory of elastic plates. *Appl. Mech. Rev.*, vol. 38, pp. 227–233.

**Ribbens, C. J.** (1989): A fast adaptive grid scheme for elliptic partial differential equations. *ACM Trans. Math. Software*, vol. 15, pp. 179–197.

**Rivara, M. C.** (1984): Algorithms for refining triangular grids suitable for adaptive and multigrid techniques. *Internat. J. Numer. Meth. Engrg.*, vol. 20, pp. 745–756.

**Rosenberg, I. G.; Stenger, F.** (1975): A lower bound on the angle of triangles constructed by bisecting the longest side. *Math. Comp.*, vol. 29, pp. 390–395.

**Verfürth, R.** (1996): *A review of a posteriori error estimation and adaptive mesh-refinement techniques*. Wiley-Teubner, Chichester - New York - Stuttgart.

**Yasamura, K. Y.; Stowe, T. D.; Chow, E. M.; Pfafman, T.; Kenny, T. W.; Rugar, D.** (1998): A study of microcantilever quality factor. In *Solid-State Sensor and Actuator Workshop*, Hilton Head Island, South Carolina.

**Zienkiewicz, O. C.; Taylor, R. L.** (1989): *The finite element method*. McGraw-Hill, London.

**Zienkiewicz, O. C.; Zhu, J. Z.** (1987): A simple error estimator and adaptive procedure for practical engineering analysis. *Int. J. Numer. Meth. Engrg.*, vol. 24, pp. 337–357.